JAAS

Accepted Manuscript

This is an *Accepted Manuscript*, which has been through the Royal Society of Chemistry peer review process and has been accepted for publication.

Accepted Manuscripts are published online shortly after acceptance, before technical editing, formatting and proof reading. Using this free service, authors can make their results available to the community, in citable form, before we publish the edited article. We will replace this *Accepted Manuscript* with the edited and formatted *Advance Article* as soon as it is available.

You can find more information about *Accepted Manuscripts* in the Information for Authors.

Please note that technical editing may introduce minor changes to the text and/or graphics, which may alter content. The journal's standard Terms & Conditions and the Ethical guidelines still apply. In no event shall the Royal Society of Chemistry be held responsible for any errors or omissions in this *Accepted Manuscript* or any consequences arising from the use of any information it contains.

ROYAL SOCIETY OF CHEMISTRY

www.rsc.org/jaas

Phase-selective LIBS with secondary resonant excitation demonstrates strongly-enhanced emission in the in-situ study of flame synthesis of titania nanoparticles.

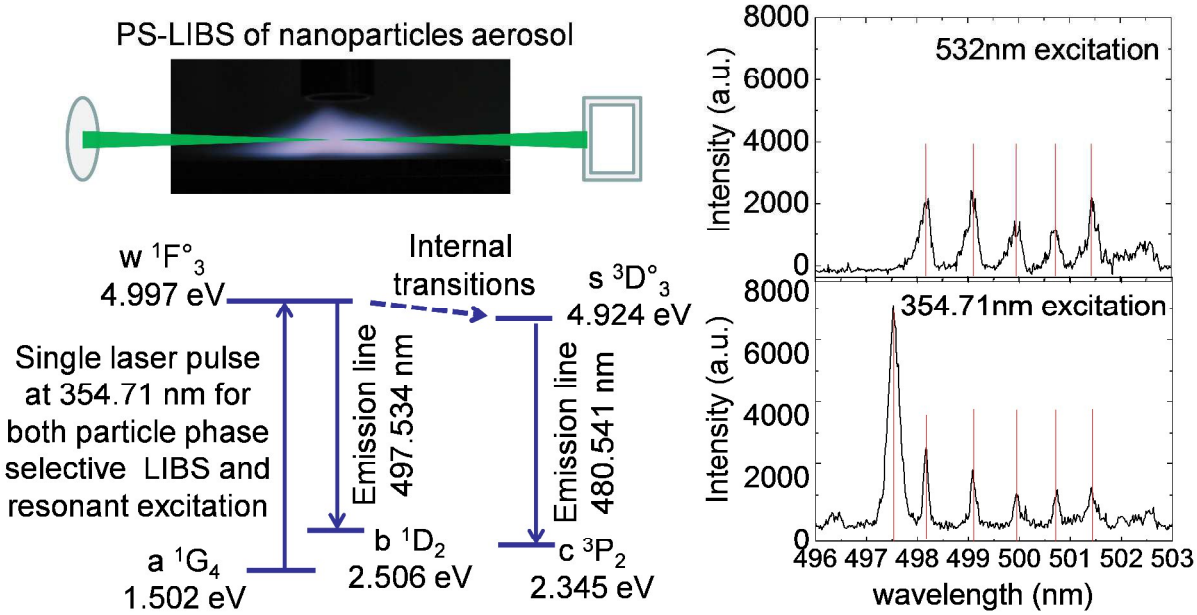

Journal of Analytical Atomic Spectrometry Accepted Manuscript

Phase-selective laser-induced breakdown spectroscopy of metal-oxide nanoparticle aerosols with secondary resonant excitation during flame synthesis

Gang Xiong[1], Shuiqing Li[2], Yiyang Zhang[3], Steven G. Buckley[4], and Stephen D. Tse[1*]

[1]Department of Mechanical and Aerospace Engineering, Rutgers, The State University of New Jersey, Piscataway, NJ 08854, USA

[2]Key Laboratory for Thermal Science and Power Engineering of Ministry of Education, Department of Thermal Engineering, Tsinghua University, Beijing 100084, China

[3]Collaborative Innovation Center of Advanced Nuclear Energy Technology, Institute of Nuclear and New Energy Technology, Tsinghua University, Beijing 100084, China

[4]TSI, Inc., Redmond, WA 98052, USA

*corresponding author: sdytse@rutgers.edu

Journal of Analytical Atomic Spectrometry Accepted Manuscript

Abstract

Low-intensity phase-selective laser induced breakdown spectroscopy (PS-LIBS) with secondary resonant excitation from the same single laser pulse is employed in the *in-situ* study of flame synthesis of TiO_2 nanoparticles. Excitation from the third harmonic (i.e. 354.71 nm as measured) of an injection-seeded Nd:YAG laser breaks down flame-synthesized titanium-dioxide nanoparticles *in-situ* into their elements and then subsequently resonantly excites the titanium electrons. With low-intensity laser excitation (~30 mJ/pulse or 2.4 GW/cm^2), only the

nanoparticle phase is selectively broken down, forming nano-plasmas without any observable Bremsstrahlung radiation. The induced emission at 497.534 nm resulting from the secondary resonant Ti excitation is markedly stronger than other/primary emissions. Compared to 532 nm excitation (with no secondary resonant excitation), where atomic emission intensity saturates at a laser power of ~20 mJ/pulse (1.6 GW/cm^2 irradiance), the emissions from 354.71 nm excitation exhibit no saturation with laser irradiance because of the secondary resonant excitation, until gas-phase breakdown occurs at a laser power of 40 mJ/pulse (3.2 GW/cm^2 irradiance). Temporal evolutions of the emissions are also studied, revealing that the 497.534 nm emission maximizes earlier, but is shorter lived. Interestingly, transient line splitting with dependence on excitation laser wavelength is observed and investigated. Additional experiments scanning the excitation laser wavelength around other resonant excitation lines show that the emission intensity can be enhanced by about 130 times at 282.347 nm excitation. Thus, using the secondary resonant excitation effect, detection thresholds could be remarkably improved for phase-selective measurements of nano-aerosols.

Key words: resonant laser induced breakdown spectroscopy (LIBS); phase selective; flame synthesis; nanoparticles

1. Introduction

Laser induced breakdown spectroscopy (LIBS) has been applied extensively to analyze solids, liquids, gases, and aerosols in various environments [1–4]. LIBS has become a very popular analytical method owing to its unique features such as no (or minimal) sample preparation, applicability to almost any type of sample in almost any environment, capability for *in-situ* measurements, and speed of analysis. LIBS analyses on aerosols have been employed in many

Journal of Analytical Atomic Spectrometry Accepted Manuscript

conditions, such as coal gasification [5], ambient environments [6], experimentally-controlled settings [7,8], and single-particle systems [9]. There have been efforts at gaining better understanding and at extending the capability of LIBS on aerosols. Hybl et al. [10] differentiated biological agents from natural background aerosols based on ratios of the atomic lines. Mukherjee et al. [11] applied LIBS to determine the extent of oxidation or coating thickness of aluminum nanoparticles. Diwakar et al. [12,13] developed a near real-time measurement of elemental compositions of aerosols of 30-900nm size at low concentrations by collecting particles onto a flat-tip microneedle electrode and then performing LIBS on the needle tip. Thärnhage et al. [14] augmented LIBS with a trigger system such that the laser was fired only when a particle was expected in the focal zone, thus significantly increasing the hit rate for detection and classification of micrometer-sized single particles in real-time. Fortes et al. [15] combined optical catapulting (OC) and optical trapping (OT) with LIBS, permitting separation and manipulation of particles in a heterogeneous mixture, with subsequent analysis of the isolated particle of interest by changing the condition of optical trapping. Along with other various key laser-based diagnostics [16–19], LIBS has been applied widely in combustion processes, e.g., to monitor the release of elements [20], and to study mixing and other phenomena [21].

In our previous work [22], a novel low-intensity phase-selective laser-induced breakdown spectroscopy (PS-LIBS) method for nanoparticle detection during flame synthesis was developed. We demonstrated that unlike the processes based on conventional LIBS for aerosols as referenced above, the laser fluence is appropriately low so that only a nanoplasma is created from each nanoparticle with no gas-phase breakdown or macroscopically-observable spark. Moreover, the breakdown occurs only when nanoparticles are ablated, allowing

Journal of Analytical Atomic Spectrometry Accepted Manuscript

distinguishment of the elements from the solid particle phase. Thus, this technique is particularly helpful in understanding the gas-to-particle transition process. Further development has been achieved for two-dimensional imaging of gas-to-particle transition and *in-situ* measurement of volume fractions of metal-oxide nanoparticles in a flow field by using the second harmonic mode (532nm) of the Nd:YAG laser [23]. The absorption-ablation-excitation mechanism in laser-cluster interactions of the low-intensity PS-LIBS process has been scrutinized by comparing Rayleigh scattering versus atomic emission of aerosol clusters in this regime by using both first and second harmonic modes [24]. In contrast to elastic or inelastic scattering at lower laser irradiance ($< 10^{-4}$ GW/cm^2), using PS-LIBS, particles are ablated at a laser irradiance above a critical threshold but below that for gas-phase breakdown. Noteworthy, this threshold is significantly influenced by the photon energy and the bandgap of the nanoparticulates. When the photon energy is not high enough to excite the electrons, higher laser irradiance is needed to ensure the possibility of multi-photon excitation. For example, under the same nanoparticle flame-synthesis condition, atomic emission occurs when the 1064 nm laser irradiance exceeds an onset intensity of 1 GW/cm^2, which is about six times higher than that for 532 nm excitation. However, the atomic emission with 1064 nm laser excitation is much weaker—about one to two orders of magnitude lower than that for 532 nm excitation at the same intensity [24]. Further clarification of the underlying physics of PS-LIBS should involve studies at shorter excitation laser wavelengths, e.g. 355 nm, corresponding to energies above the bandgaps of the materials of interest.

In the current work, the effect of excitation wavelength is investigated using the third harmonic of the Nd:YAG laser in low-intensity PS-LIBS instead of the second harmonic as done in previous research. Interestingly, PS-LIBS with subsequent resonant excitation is observed.

Journal of Analytical Atomic Spectrometry Accepted Manuscript

With low-intensity excitation (~30 mJ/pulse or 2.4 GW/cm^2 irradiance), only the particle phase is selectively broken down, and the induced emission from the subsequent resonant excitation of the constituent Ti (now in plasma phase) is markedly stronger than other emissions. The generality of this single pulse PS-LIBS with secondary resonant excitation technique is demonstrated by scanning the excitation wavelength near different resonant lines of Ti to verify the enhanced emission effect. For excitation near 282nm, the resonant emission intensity can be increased by about a factor of 130, demonstrating the capability to achieve a very low limit of detection for element(s) of interest from the nanoparticle phase, when the excitation wavelength can be selected.

2. Experimental setup

A stagnation swirl flame setup is utilized to synthesize TiO_2 nanoparticles, as shown in Fig. 1. The details of the setup can be found in Refs. [22,25]. In brief, the burner consists of an 18-mm diameter stainless-steel nozzle with an internal swirler, and a stagnation substrate (temperature controlled) situated 19-mm downstream. Premixed CH_4, O_2 and N_2 flow into the burner, sustaining a premixed flame, while a portion of the N_2 (2 L/min) runs through a bubbler containing titanium tetraisopropoxide (TTIP) precursor and carries the precursor to the flame. The precursor pyrolyzes and oxidizes in the flame forming supersaturated metal-oxide vapor that condenses into nanoparticles as the gases cool upon reaching the cold substrate [26,27]. TiO_2 nanoparticles ~10 nm in size are formed under the given conditions.

The setup for the laser-based diagnostics is shown in Fig. 2. An injection-seeded Nd:YAG laser that can operate at second (532nm) or third (355nm) harmonic modes serves as the excitation source. The output laser beam is focused by a 500-mm focal-length plano-convex

Journal of Analytical Atomic Spectrometry Accepted Manuscript

fused silica lens to the region of interest in the flame-generated nano-aerosol. The collection optics consist of two 400-mm focal-length achromats, an image rotator, and turning mirrors. The emissions are collected at 90° into a triple spectrometer (Princeton Instruments TriVista), which is composed of two 0.5m spectrometers and one 0.75m spectrometer, all with 1800 groove/mm holographic gratings. The triple spectrometer can work in additive mode (which gives high spectral resolution), subtractive mode (which gives high stray light rejection), or single mode (where each stage serves as a stand-alone spectrometer). In additive mode, the gratings on all 3 stages contribute to positive light dispersion. In subtractive mode, the first and second stages work as a tunable bandpass filter, where the first stage disperses light so that only a selected band passes through the slit entering the second stage which recombines the dispersed light (with a counter-oriented grating) to focus on the slit either entering the third stage or outputting to a detector. If a third stage is utilized, then it defines the spectral resolution, with output to the detector. These modes can be switched by software control.

An ICCD camera (Princeton Instruments PIMAX 3) detects the signal with selected delay and gate timing to minimize background interference and to study the temporal evolution of the process. A photomultiplier tube (PMT, Hamamatsu R928) is connected to the spectrometer at another port, with its signals recorded by a digital oscilloscope (Agilent Infiniium 54845A oscilloscope, 1.5 GHz sampling rate), and further assesses the temporal evolution of the emissions at selected wavelengths. The typical slit width is set to 50-200 μm to minimize instrumental broadening and to obtain appropriate spatial and spectral resolutions.

3. Results and discussions

Journal of Analytical Atomic Spectrometry Accepted Manuscript

To achieve high stray light rejection along with appropriate spectral resolution, the triple spectrometer first runs in subtractive mode, where the first two stages work as a band pass filter and the third stage works as the main spectrometer. The entrance slit is set to 200 μm. The emission spectra from 532 nm and 355 nm laser excitation at 14mm away from the burner exit are shown in Fig. 3. The laser irradiance is 2.4 GW/cm^2 for both cases at 10Hz repetition rate with ~10 ns pulse width; and the signal collection time is 150 seconds (1500 shots) with 400 ns gate width to capture the whole signal emission duration.

For 532 nm excitation, the results are consistent with our previous work [22], with Ti (I) atomic emission lines at 498.173 nm, 499.107 nm, 499.950 nm, 500.721 nm, and 501.428 nm identified and no Bremsstrahlung background detected. However, for 355 nm excitation, a new strong emission line at 497.534 nm appears. As will be discussed, this line corresponds to the Ti (I) atomic line produced by the transition from upper $3d^3(^2D2)4p$ level $w^1F°_3$ to lower $3d^3(^2D2)4s$ level b^1D_2. The line strength can be calculated from the expression [1]:

$$I = \frac{h\nu A_{ij} N_0 g}{4\pi Z} \exp(-\frac{E_j}{kT}) \quad (1)$$

where I is the emission intensity (W/sr); h is Planck's constant; v is the frequency; A_{ij} is the transition probability (with Einstein A coefficient) from the upper level j to the lower level i with energy difference of hv; N is the absolute number density of the atoms at upper level j; N_0 is the total number of atoms; Z is the partition function, usually taken as the statistical weight of the ground level; E_j is the energy of the upper level; g is the statistical weight of energy level j; k is Boltzmann's constant; and T is the plasma temperature.

Journal of Analytical Atomic Spectrometry Accepted Manuscript

Based on the data from the National Institute of Standards and Technology (NIST) [28] and Wiese and Fuhr [29], and assuming a local thermodynamic equilibrium (LTE) plasma temperature of 10,000 K (or 20,000K), which is in the characteristic temperature range of LIBS, the non-resonant emission intensity at 497.534 nm should be less than 10% (or 20%) of the emission intensity at 498.173 nm. In fact, the experimentally observed emission intensity at 497.534nm is 50 (or 25) times greater than what it is predicted under LTE conditions assuming a 10,000K (or 20,000K) plasma temperature, indicating another mechanism (i.e. resonance) at play beyond traditional LIBS or previously-studied PS-LIBS. Moreover, the strength of the new resonant emission is shown clearly by the comparison of the emission intensity spectra for 532nm and 355nm excitations, at the same fluence, in Fig. 3. Compared to the existing strong emission at 498.173nm, for both 532nm and 355nm excitations, this new emission at 497.534 nm is about 5 times stronger. As such, the sensitivity of previously-studied PS-LIBS can be improved by using the secondary resonance effect. To confirm that the 497.534 nm line is from Ti atomic emission, rather than from intermediate species in the combustion and decomposition processes during flame synthesis, inert aerosolized Ti particles are examined. Ti particles are generated using a spark generator as described in the work by Byeon et al. [30]. Two titanium rods serve as electrodes, and 3kV difference is applied to the rods in an argon atmosphere, producing sparks/particles. Using focused 355nm excitation with laser irradiance of 2.4 GW/cm^2, strong emission at 497.534 nm is reproduced, confirming that the emission line is indeed from atomic titanium.

As mentioned above, the 497.534 nm emission corresponds to the Ti (I) atomic line produced by the transition from upper $3d^3(^2D2)4p$ level $w^1F°_3$ to lower $3d^3(^2D2)4s$ level b^1D_2. The '355 nm' laser line is actually measured to be 354.71 nm, equivalent to one-third of the

Journal of Analytical Atomic Spectrometry Accepted Manuscript

fundamental wavelength of the Nd:YAG laser at 1064.13 nm, which is consistent with the value from the literature [31]. Coincidentally, this laser line matches the Ti (I) absorption line at 354.703nm, with the upper level of this line being exactly the upper level of the 497.534 nm transition line, such that the electrons can be excited to the upper $3d^3(^2D2)4p$ level $w^1F°_3$, as shown in the Fig. 4. Besides the direct emission from the $w^1F°_3$ level, there can also be some internal transitions to other states, as 480.541 nm emission (upper level $s^3D°_3$, with energy slightly lower than from the $w^1F°_3$ level) is also observed with high intensity.

There are several relevant mechanisms for describing this phenomenon, namely LIBS with laser-induced fluorescence (LIBS-LIF), resonant enhanced laser induced breakdown spectroscopy (RELIBS), and resonant laser induced breakdown spectroscopy (RLIBS). For LIBS-LIF, one laser pulse creates the plasma and another pulse excites selected states to produce fluorescence [32–35]. Two laser pulses, usually two lasers, are employed, which may result in system complexity. For RELIBS, one pulse performs the ablation and another pulse resonantly excites atoms, along with rekindling the plasma. A delay time of 30 ns or more relative to the second pulse is needed for signal collection [36,37]. For the RLIBS technique [38–42], which is a combination of resonant laser ablation (RLA) [43–46] and optical emission detection, only one laser pulse of selected wavelength is employed to create the plasma and also excite the electrons resonantly. In the RLIBS process, the first-come photons ablate the sample and then the other photons resonantly excite and ionize the vapor [47]. There are also some enhanced desorption for the ablation process [48], exothermic collision for vapor heating and reaching LTE [49], and transition of the energy from excited species to other components [39]. Based on the energy levels and the description of these three mechanisms, our observed phenomenon is most related to the RLIBS mechanism, with the 354.71 nm laser ablating the samples and then resonantly

Journal of Analytical Atomic Spectrometry Accepted Manuscript

exciting the electrons of Ti atoms from a^1G_4 level to $w^1F°_3$ level. The excited electrons then undergo radiation processes, transitions, and exothermic collisions. It is worth noting that the a^1G_4 level is not the ground level of Ti, and thus the number of electrons in this level is not very large compared to that in the low-energy levels, which means that the signal can be enhanced, upon strategically selecting the excitation laser line.

RLIBS and RLA have been applied to major and trace element detections, manifesting part-per-billion sensitivity [38,45,46,50] and potential for quantitative measurements [41]. Some modeling work has been done to better understand the process [51]. However, for all the literature found, the RLIBS and RLA have been done with solid bulk samples or pure gas vapor. The current work presents the first study of the RLIBS effect in nanoparticle aerosols. More importantly, combining resonant ablation and low-intensity phase-selective LIBS will create some new features. The resonant ablation process is shown to be capable of selectively ionizing different target analytes from the same composite sample [50,52]. Combined with the low-intensity PS-LIBS on nanoparticles, it is possible to perform phase-selective and analyte-selective LIBS with low detection limits.

However, the diagnostic also needs to consider the possible direct excitation of "target" atoms already in the gas phase, e.g. Ti, prior to interaction with the laser. Here, an initial scan at very low laser excitation intensity below the ablation threshold for pure Ti nanoparticles should divulge the presence of any "pre-existing" atomic Ti that would be excited directly by the 354.71 nm laser. If such is the case, then non-resonant excitation, e.g. 532nm, should be used for PS-LIBS. Nevertheless, in diagnosing specific systems, such as flame synthesis of metal oxides, the presence of pure metal atoms in the post-flame gases would be almost non-existent, especially for lean flames (as in our setup here), where the goal is to produce the metal oxide. Only in a

Journal of Analytical Atomic Spectrometry Accepted Manuscript

specially-tailored highly-reducing environment would such metal atoms be found. Notwithstanding, proper application of the PS-LIBS with secondary resonant excitation diagnostic would require understanding of the given system's innate synthesis characteristics, along with perhaps other techniques to discriminate any concurrent effects.

To demonstrate phase-selectivity, emission intensities along the centerline axis of the synthesis flow from 532 nm and 355 nm laser excitations are presented in Fig. 5. The calculated diameter from a simple monodisperse population balance model [22] is also displayed to indicate the expected phase-change or particle growth along the axis. The 'total' intensities are calculated by integrating the emission from 497 nm to 502 nm. The emission intensities for 355nm excitation show quick increases at 5-12 mm downstream from the burner exit, where the flame region is located, indicating phase change and particle growth. Parenthetically, the trend of the increasing emission signal along the centerline axis of the flow field (Fig. 5) further confirms that we are identifying TiO_2 nanoparticles in our lean flame synthesis system, as Ti-containing species convert to TiO_2 particles and grow along the axis [53]. In contrast, if Ti atoms existed prior to laser-induced breakdown of the nanoparticles, then their direct excitation would have instead resulted in decreasing emission along the axis. Moreover, for 354.702 nm excitation, the lower energy level of Ti (a^1G_4, 1.502eV) of the excitation process is not at the ground state, which can be beneficial since the fraction of atoms at this state at the temperatures of the post-flame gas is very low without excitation by the laser-induced plasma. Nonetheless, differences exist for these two excitation wavelengths. At 2 mm downstream from burner exit (before particle growth), there is no emission around 500nm for 532nm excitation, while there exists emission for 355 nm excitation, albeit with low intensity. Since in this low-swirl flame burner the gases and precursor are pre-mixed prior to the burner exit, the TTIP precursor

Journal of Analytical Atomic Spectrometry Accepted Manuscript

encounters O_2, and there will be some reaction in the gas phase at ~ 100℃ to form some TiO_2 monomers/clusters at the burner exit, eventually producing TiO_2 particles at longer residence times [54,55]. These clusters may absorb the 355 nm laser light and be excited and broken down, while the 532 nm laser light is not absorbed much, attributable to different absorption efficiencies for the different wavelengths [56,57]. Because some of the Ti-containing species do not have large enough absorption cross section, they will not interact as 'particles' with the excitation laser beam for certain wavelengths; and the emitted signal will increase until these gas-phase species grow to become 'particles' at a specific size (d_0). Then, they will be selectively broken down (with no gas phase breakdown). The d_0 will be different for different excitation wavelengths, as shown in Fig. 5. For example, at the initial stage, some species are excited by 355nm excitation, but not by 532nm. Such emission is related to the plasma production and strong emission from it. The dissimilar cluster/particle size detection threshold may be further developed to become a quantitative method for size characterization.

To further investigate the characteristics of PS-LIBS with resonant 355 nm excitation on nanoparticles, the emission intensity change with laser irradiance is studied, as exhibited in Fig. 6. The inset compares the emission intensity change at 532 nm laser excitation. For both cases, the measured location is 14 mm downstream from the burner exit with precursor concentration 116 ppm. The particle size is ~10 nm [22]. With 355 nm excitation, the laser irradiance increases from 0.04 GW/cm^2 to 2.8 GW/cm^2 without gas-phase breakdown or visible spark, which is observed at 3.2 GW/cm^2. The resonant emission at 497.534 nm can be detected and distinguished easily by the ICCD, even at 0.04 GW/cm^2 laser irradiance, corresponding to a laser fluence of 0.4 J/cm^2, which is still above the breakdown threshold for most metals [58]. Note that the ablation threshold is generally much higher for metal-oxides (given the lack of free

Journal of Analytical Atomic Spectrometry Accepted Manuscript

electrons in the conduction band) than for metals. With 532 nm excitation, the PS-LIBS emission intensity saturates at a laser power of 1.6 GW/cm^2, plateauing until gas breakdown at 5.6 GW/cm^2. Nevertheless, the emission intensities from 355 nm laser excitation exhibit no saturation, even up to gas-phase breakdown at 3.2 GW/cm^2. The saturation at 1.6 GW/cm^2 with 532nm excitation corresponds to complete ablation of the particles. In contrast, PS-LIBS with 355 nm resonant excitation can continue to excite more electrons to the $w^1F°_3$ upper level, with the upper level transitioning to other energy levels ($s^3D°_3$, b^1D_2, and others), thus leading to continuous increase of the 497.534 nm emission as well as other emissions.

The temporal evolution of the emissions at a laser irradiance of 2.4 GW/cm^2 is then investigated with gated ICCD camera and PMT. The gated ICCD camera records the emission spectrum at a gate width of 5ns with different delay times relative to the laser pulse. The PMT obtains more detailed temporal evolution for emissions in a certain wavelength range. The triple spectrometer is run in single and double mode. To obtain the temporal evolution using the ICCD with sufficient emission intensity, the camera is placed at the output of the first stage of the TriVista system; and the width of the entrance slit is set to 50 μm. For the PMT setup, the PMT is placed at the output of the second stage of the TriVista system, with the first and second stages working in the double subtractive mode as a fine band pass filter (with 40 μm intermediate slit size, corresponding to a band-pass width of 0.04 nm).

The temporal evolution of the emission spectrum recorded by the ICCD camera from relative delay time 2.5 to 32.5 ns (the time when the detected elastic scattering of the laser pulse from the same measurement volume reaches its maximum is set to 0) with 5 ns gate width is shown in Fig. 7. The curve at 2.5 ns relative delay time is the emission collected from 0 to 5 ns; the curve at 7.5 ns relative delay time is the emission collected from 5 ns to 10 ns, and so forth.

Journal of Analytical Atomic Spectrometry Accepted Manuscript

As a result of the property of the low-intensity PS-LIBS, the white noise is low even at 2.5 ns relative delay time. The 497.534 nm emission is fairly strong at 2.5 ns relative delay time and then decays with time until it vanishes at 27.5 ns relative delay time. However, for the other emissions, e.g. 498.173 nm, they increase from 2.5 to 12.5 ns relative delay time, and then decline gradually. They are still detectable at 32.5 ns relative delay time, but disappear by 37.5 ns relative delay time. The 497.534 nm emission decays faster than the 498.173 nm emission. As calculated above, for LTE, the 497.534 nm emission should be much weaker than the 498.173 nm emission. The high emission intensity at 497.534 nm at the early stage is due to the selective excitation by the laser, which produces more electrons in the $w^1F^0_3$ level than that for the LTE condition. However, this excited state is closely coupled to the optical pump by the laser, and will decay rapidly after the laser pulse. The timing of the rise and decay will be further elaborated upon in the discussions that follow, along with presentation of the detailed temporal emissions measured by PMT.

Intriguingly, at 2.5 ns relative delay time (peak of the laser excitation), the emission at 497.534 nm is composed of two peaks, and this is further investigated close to the onset of the laser pulse, i.e., from -7.5 ns to 2.5 ns relative delay, as shown in Fig. 8. At -7.5 ns relative delay time, there are two peaks straddling 497.534 nm, distinct from each other. At -2.5 ns relative delay time, the intensity of the emissions increases, and the two peaks get closer together. At 2.5 ns relative delay time, the two peaks get even closer, but are still distinguishable from each other. The two peaks are fitted with Lorentzian profile, and the center wavelength evolution is shown in the inset of Fig. 8. The two peaks are 0.3 nm away from each other at -7.5 ns relative delay time (for emissions collected from -10ns to -5ns, where at -5ns time the laser intensity is half of the

Journal of Analytical Atomic Spectrometry Accepted Manuscript

maximum intensity), about 0.15 nm from 497.5 nm on both sides. Thereafter, they move towards 497.53 nm, and merge into a single peak at 7.5 ns relative delay time.

It is possible that this splitting is due to the influence of the magnetic field via the Zeeman effect. Magnetic field generated in laser-induced plasma has been observed since the early 1970s [59] and is shown to be about coincident with the laser pulse [60]. The Zeeman effect has been employed to determine the strengths of magnetic fields [60–62]. Based on the energy difference of the split peaks, the configuration of the electrons [28], and the formula given by Drake [63], the temporal magnetic field is calculated to be 2.8 T, 1.4 T, and 0.3 T, at -7.5 ns, -2.5 ns, and +2.5 ns relative delay time, respectively. These field strengths may seem exceedingly large, but are actually consistent with the values given by McLean et al. [60], for laser power at this range. However, as seen from Figs. 8 and 9, the split peaks are farthest apart before the detected laser pulse has reached its maximum intensity, which is not expected as the magnetic field should be correspondingly large for the Zeeman effect. Yet, it is worth noting again that the laser pulse characterized here is actually elastic scatter from the same measurement volume as from the other emissions, using the same collection optics, triple spectrometer, and detector, but with the gratings turned to the laser excitation wavelength. Although we assume that the Rayleigh scatter is instantaneous [64], matching the excitation laser pulse, other effects may come into play, affecting its temporal nature, given the early breakdown of the nanoparticle phase. For example, the corresponding electric field from the laser is large enough to breakdown the nanoparticles and form nanoplasmas, despite also being early in the laser pulse process. Moreover, the exact temporal evolution of the magnetic field may not be the same as that for the laser pulse under this condition. The generated magnetic field depends strongly on the laser-matter-plasma interactions [59,65,66]; and especially in the present case, the mass of the

Journal of Analytical Atomic Spectrometry Accepted Manuscript

nanoparticles will be reduced quickly within the first several nanoseconds [24], which will influence the magnetic field generated. Nevertheless, this line-splitting phenomenon is very interesting, and needs further investigation.

Detailed temporal responses captured by the PMT detector for different wavelengths are given in Fig. 9. The emissions around 497.53 nm are examined to show the detailed evolution of different wavelengths, i.e., from 497.35 nm to 497.70 nm at 0.05 nm intervals, to show the detailed evolution of the fine structure around 497.534nm, and to confirm the peak splitting. The evolution of emission centered at 498.17 nm is also displayed for comparison. The pulse width (FWHM, full width at half maximum) of the laser is fitted to be 10 ns, and the time when the laser pulse reaches its maximum is set to zero. The emissions around 497.53 nm increase rapidly when the laser pulse is present. However, the 498.17 nm emission rises slowly but lasts for a longer duration. The sequence when the emissions reach their peaks is shown in Fig. 10. Relative to the laser pulse peak, the emissions around 497.53 nm maximize about 3 to 6 ns later, while the 498.17 nm emission maximizes about 12 ns later. The emissions around 497.53 nm maximize 6-9 ns prior to the emission around 498.17 nm. The emissions at 497.35nm and 497.70nm maximize at ~3ns after the laser peak, but this time value increases monotonically to 6ns as the peaks of the other emissions converge toward 497.53nm from either side. If the time for all the emissions to maximize were the same, then only a single integrated peak would result. Thus, this sequence of the peaks for the different emissions again corroborates the splitting. The laser excites the electrons resonantly, leading to fast increase in emission at 497.53 nm. However, this emission is highly dependent on laser presence and decays as the laser pulse diminishes. After the laser pulse ends at ~15 ns, the emissions around 497.53 nm last for another

Journal of Analytical Atomic Spectrometry Accepted Manuscript

15 ns, corresponding approximately to the transition decay time for the Ti (I) 497.534 nm line, which is on the order of $1/A_{ij} \approx 16$ ns based on the data given by Wiese and Fuhr [29].

Another interesting phenomenon is the dissimilarity observed for the emissions resulting from laser excitation with and without injection seeding. For seeded laser excitation, as shown above, the 497.534 nm emission splits into two peaks with the onset of laser irradiation. On the other hand, for unseeded laser excitation, the 497.534 nm emission does not display complete splitting, but rather broadens. As presented in Fig. 11, the fitted FWHM is 0.18 nm at the beginning and then decays with time. The cumulative emission spectrum collected from -10 ns to -5 ns relative delay times is shown in the inset. From 25 ns to 30 ns, the emission at 497.534 nm vanishes, which is the same as for the seeded case. Furthermore, the 480.54 nm emission is 4 times stronger for the excitation with unseeded versus seeded laser. We currently cannot provide a good explanation for this phenomenon, and additional research is required.

Finally, to demonstrate the generality and to quantify the signal augmentation of the effect of secondary resonant excitation by the same laser pulse, a tunable dye laser (Sirah PrecisionScan) pumped by the second harmonic (532nm) of an Nd:YAG laser (Quanta-Ray LAB 170, Spectra Physics) is employed to investigate the dependence of emission intensity on excitation laser wavelength. The frequency of the output of the dye laser is then doubled passing through a KDP (potassium dihydrogen phosphate) crystal. The LambdaLock feature ensures accurate control of the laser wavelength to less than ±2.5 pm. The wavelength of the laser is tuned around one atomic line of Ti (I) at 282.347nm (lower state $3d^24s^2$, energy level a^3F_3, higher state $3d^3(^4P)4p$, energy level $w^5D°_2$). The laser energy is 7 mJ/pulse and is focused by a 150mm focal-length fused-silica plano-convex lens to conduct PS-LIBS with secondary resonant excitation. The results are shown in Fig. 12 for different excitation laser wavelengths. The

Journal of Analytical Atomic Spectrometry Accepted Manuscript

emission lines around 450 nm and 500 nm are strong at 282.22 nm laser excitation, while the emissions around 460 nm are fairly weak. When the excitation laser line is tuned close to the resonant excitation line at 282.347 nm, the emissions around 460 nm increase dramatically. Closer inspection divulges that the strongest emissions around 460 nm are actually 462.934 nm and 463.936 nm, both from emissions with upper energy level $w^5D°_2$. The intensity of the emission lines at 463.936 nm increases from less than 500 au (almost at the noise level in this case) to 65,000 au. This large enhancement establishes the potential to improve emission signals considerably with well-selected excitation laser lines for a given elemental composition of interest.

4. Concluding Remarks

Low-intensity PS-LIBS with secondary resonant excitation from the same single laser pulse is employed in the *in-situ* study of flame synthesis of TiO_2 nanoparticles. Besides the phase-selectivity property of the low-intensity LIBS, the new emission at 497.534 nm, caused by secondary resonant excitation from the same single laser pulse (~355 nm), is found to be much stronger than other/primary emissions. Because of the continuous resonant excitation of the atoms, the emissions show no plateauing as they do with 532 nm laser excitation. The 497.534 nm emission is highly dependent on laser presence, maximizing prior to other emissions and decaying fast as the laser pulse diminishes. The temporal evolution of the emissions also evinces that the 497.534 nm emission splits into two lines at early times, which may be due to the magnetic field generated by the laser pulse via the Zeeman effect; however additional investigation is needed.

Journal of Analytical Atomic Spectrometry Accepted Manuscript

The combination of phase-selective LIBS and resonant LIBS on nanoparticles measurement leads to a high-intensity signal for particle phase detection. The technique has the potential to make elemental measurements of nanoparticles at very-low detection limits, as well as phase-selective analyte-selective measurements. As shown by scanning the excitation wavelength, other resonant lines not only show the same effect, but also result in emission lines that are exceedingly strong (i.e. enhanced by 130 times), suggesting that the technique is widely applicable. With short focal-length lenses, laser power can be lowered significantly while still maintaining strong signal. This setup can even be utilized with micro-LIBS technique [67–69] to improve detection limit. In conjunction with the resonant LIBS process, there is also possibility to create lasing. Mirrorless lasing has been performed in air [70] and metal vapors [71]; and lasing with titanium vapor at different wavelengths have been examined [72–75]. With long focal-length lenses, far-distant remote detection with high signal intensity can be realized if backward emission lasing occurs, which is the subject of on-going work.

Acknowledgements

This work was supported by the Army Research Office through grants W911NF-08-1-0417, W911NF-09-1-0138, and W911NF-10-1-0018. Support from the National Natural Science Funds of China (No. 51176094) is acknowledged for co-author SQL. Special thanks are due to Ms. Aditi Kulkarni at Rutgers for assistance with flame synthesis and to Prof. Jeong Hoon Byeon at Yeungnam University, South Korea, for help with spark synthesis.

Journal of Analytical Atomic Spectrometry Accepted Manuscript

References

1. D. A. Cremers and L. J. Radziemski, *Handbook of Laser-Induced Breakdown Spectroscopy* (John Wiley & Sons, 2006).
2. A. W. Miziolek, V. Palleschi, and I. Schechter, *Laser-Induced Breakdown Spectroscopy (LIBS) Fundamentals and Applications* (Cambridge University Press, 2006).
3. D. W. Hahn and N. Omenetto, "Laser-induced breakdown spectroscopy (LIBS), part I: Review of basic diagnostics and plasma–particle interactions: Still-challenging issues within the analytical plasma community," Appl. Spectrosc. **64**, 335A–366A (2010).
4. D. W. Hahn and N. Omenetto, "Laser-Induced Breakdown Spectroscopy (LIBS), Part II: Review of Instrumental and Methodological Approaches to Material Analysis and Applications to Different Fields," Appl. Spectrosc. **66**, 347–419 (2012).
5. L. J. Radziemski, T. R. Loree, D. A. Cremers, and N. M. Hoffman, "Time-resolved laser-induced breakdown spectrometry of aerosols," Anal. Chem. **55**, 1246–1252 (1983).
6. J. E. Carranza, B. T. Fisher, G. D. Yoder, and D. W. Hahn, "On-line analysis of ambient air aerosols using laser-induced breakdown spectroscopy," Spectrochim. Acta Part B At. Spectrosc. **56**, 851–864 (2001).
7. R. G. Pinnick, P. Chýlek, M. Jarzembski, E. Creegan, V. Srivastava, G. Fernandez, J. D. Pendleton, and A. Biswas, "Aerosol-induced laser breakdown thresholds: wavelength dependence," Appl. Opt. **27**, 987–996 (1988).
8. D. W. Hahn and M. M. Lunden, "Detection and Analysis of Aerosol Particles by Laser-Induced Breakdown Spectroscopy," Aerosol Sci. Technol. **33**, 30–48 (2000).
9. D. W. Hahn, "Laser-induced breakdown spectroscopy for sizing and elemental analysis of discrete aerosol particles," Appl. Phys. Lett. **72**, 2960–2962 (1998).

Journal of Analytical Atomic Spectrometry Accepted Manuscript

10. J. D. Hybl, G. A. Lithgow, and S. G. Buckley, "Laser-Induced Breakdown Spectroscopy Detection and Classification of Biological Aerosols," Appl. Spectrosc. **57**, 1207–1215 (2003).

11. D. Mukherjee, A. Rai, and M. R. Zachariah, "Quantitative laser-induced breakdown spectroscopy for aerosols via internal calibration: Application to the oxidative coating of aluminum nanoparticles," J. Aerosol Sci. **37**, 677–695 (2006).

12. P. Diwakar, P. Kulkarni, and M. E. Birch, "New Approach for Near-Real-Time Measurement of Elemental Composition of Aerosol Using Laser-Induced Breakdown Spectroscopy," Aerosol Sci. Technol. **46**, 316–332 (2012).

13. P. K. Diwakar, K. H. Loper, A.-M. Matiaske, and D. W. Hahn, "Laser-induced breakdown spectroscopy for analysis of micro and nanoparticles," J. Anal. At. Spectrom. **27**, 1110 (2012).

14. T. Tjärnhage, P.-Å. Gradmark, A. Larsson, A. Mohammed, L. Landström, E. Sagerfors, P. Jonsson, F. Kullander, and M. Andersson, "Development of a laser-induced breakdown spectroscopy instrument for detection and classification of single-particle aerosols in real-time," Opt. Commun. **296**, 106–108 (2013).

15. F. J. Fortes, A. Fernández-Bravo, and J. J. Laserna, "Chemical characterization of single micro- and nano-particles by optical catapulting–optical trapping–laser-induced breakdown spectroscopy," Spectrochim. Acta Part B At. Spectrosc. **100**, 78–85 (2014).

16. C. Schulz and V. Sick, "Tracer-LIF diagnostics: quantitative measurement of fuel concentration, temperature and fuel/air ratio in practical combustion systems," Prog. Energy Combust. Sci. **31**, 75–121 (2005).

17. X. Liu, M. E. Smith, and S. D. Tse, "In situ Raman characterization of nanoparticle aerosols during flame synthesis," Appl. Phys. B **100**, 643–653 (2010).

18. G. Skandan, Y.-J. Chen, N. Glumac, and B. H. Kear, "Synthesis of oxide nanoparticles in low pressure flames," Nanostructured Mater. **11**, 149–158 (1999).

Journal of Analytical Atomic Spectrometry Accepted Manuscript

19. C. J. Damm, D. Lucas, R. F. Sawyer, and C. P. Koshland, "Real-Time Measurement of Combustion Generated Particles with Photofragmentation-Fluorescence," Appl. Spectrosc. **55**, 1478–1482 (2001).

20. P. J. van Eyk, P. J. Ashman, Z. T. Alwahabi, and G. J. Nathan, "Quantitative measurement of atomic sodium in the plume of a single burning coal particle," Combust. Flame **155**, 529–537 (2008).

21. J. Kiefer, Z. Li, and M. Alden, "Laser-induced breakdown spectroscopy in a partially premixed turbulent jet flame," Meas. Sci. Technol. **24**, 075205 (2013).

22. Y. Zhang, G. Xiong, S. Li, Z. Dong, S. G. Buckley, and S. D. Tse, "Novel Low-Intensity Phase-Selective Laser-Induced Breakdown Spectroscopy of TiO_2 Nanoparticle Aerosols during Flame Synthesis," Combust. Flame **160**, 725–733 (2013).

23. Y. Zhang, S. Li, Y. Ren, Q. Yao, and S. D. Tse, "A new diagnostic for volume fraction measurement of metal-oxide nanoparticles in flames using phase-selective laser-induced breakdown spectroscopy," Proc. Combust. Inst. **35**, 3681–3688 (2015).

24. Y. Ren, S. Li, Y. Zhang, S. D. Tse, and M. B. Long, "Absorption-Ablation-Excitation Mechanism of Laser-Cluster Interactions in a Nanoaerosol System," Phys. Rev. Lett. **114**, 093401 (2015).

25. J. Wang, S. Li, W. Yan, S. D. Tse, and Q. Yao, "Synthesis of TiO_2 nanoparticles by premixed stagnation swirl flames," Proc. Combust. Inst. **33**, 1925–1932 (2011).

26. H. Zhao, X. Liu, and S. D. Tse, "Control of nanoparticle size and agglomeration through electric-field-enhanced flame synthesis," J. Nanoparticle Res. **10**, 907–923 (2008).

27. H. Zhao, X. Liu, and S. D. Tse, "Effects of pressure and precursor loading in the flame synthesis of titania nanoparticles," J. Aerosol Sci. **40**, 919–937 (2009).

28. A. Kramida, Y. Ralchenko, J. Reader, and NIST ASD Team, *NIST Atomic Spectra Database (ver. 5.2), [Online]. Available: Http://physics.nist.gov/asd [2015, May 20]. National Institute of Standards and Technology, Gaithersburg, MD.* (2014).

Journal of Analytical Atomic Spectrometry Accepted Manuscript

29. W. L. Wiese and J. R. Fuhr, "Atomic transition probabilities for scandium and titanium (A critical data compilation of allowed lines)," J. Phys. Chem. Ref. Data **4**, 263–352 (1975).

30. J. H. Byeon, J. H. Park, and J. Hwang, "Spark generation of monometallic and bimetallic aerosol nanoparticles," J. Aerosol Sci. **39**, 888–896 (2008).

31. J. Lu, M. Prabhu, K. Ueda, H. Yagi, T. Yanagitani, A. Kudryashov, and A. A. Kaminskii, "Potential of ceramic YAG lasers," Laser Phys. **11**, 1053–1057 (2001).

32. S. L. Lui, Y. Godwal, M. T. Taschuk, Y. Y. Tsui, and R. Fedosejevs, "Detection of lead in water using laser-induced breakdown spectroscopy and laser-induced fluorescence," Anal. Chem. **80**, 1995–2000 (2008).

33. H. Loudyi, K. Rifaï, S. Laville, F. Vidal, M. Chaker, and M. Sabsabi, "Improving laser-induced breakdown spectroscopy (LIBS) performance for iron and lead determination in aqueous solutions with laser-induced fluorescence (LIF)," J. Anal. At. Spectrom. **24**, 1421–1428 (2009).

34. F. Hilbk-Kortenbruck, R. Noll, P. Wintjens, H. Falk, and C. Becker, "Analysis of heavy metals in soils using laser-induced breakdown spectrometry combined with laser-induced fluorescence," Spectrochim. Acta Part B At. Spectrosc. **56**, 933–945 (2001).

35. H. H. Telle, D. C. S. Beddows, G. W. Morris, and O. Samek, "Sensitive and selective spectrochemical analysis of metallic samples: the combination of laser-induced breakdown spectroscopy and laser-induced fluorescence spectroscopy," Spectrochim. Acta Part B At. Spectrosc. **56**, 947–960 (2001).

36. S. L. Lui and N. H. Cheung, "Minimally destructive analysis of aluminum alloys by resonance-enhanced laser-induced plasma spectroscopy," Anal. Chem. **77**, 2617–2623 (2005).

37. C. Goueguel, S. Laville, F. Vidal, M. Sabsabi, and M. Chaker, "Investigation of resonance-enhanced laser-induced breakdown spectroscopy for analysis of aluminium alloys," J. Anal. At. Spectrom. **25**, 635–644 (2010).

Journal of Analytical Atomic Spectrometry Accepted Manuscript

38. C. Goueguel, S. Laville, F. Vidal, M. Chaker, and M. Sabsabi, "Resonant laser-induced breakdown spectroscopy for analysis of lead traces in copper alloys," J. Anal. At. Spectrom. **26**, 2452–2460 (2011).

39. K. Rifai, F. Vidal, M. Chaker, and M. Sabsabi, "Resonant laser-induced breakdown spectroscopy (RLIBS) analysis of traces through selective excitation of aluminum in aluminum alloys," J. Anal. At. Spectrom. **28**, 388–395 (2013).

40. D. Cleveland, P. Stchur, and R. G. Michel, "Effect of background gas, sample angle and laser polarization on the enhancement effect of resonant laser ablation," J. Anal. At. Spectrom. **22**, 745–753 (2007).

41. D. Cleveland and R. G. Michel, "Quantitative analysis by resonant laser ablation with optical emission detection: Resonant laser-induced breakdown spectroscopy," Microchem. J. **95**, 120–123 (2010).

42. F. J. Fortes, J. Moros, P. Lucena, L. M. Cabalín, and J. J. Laserna, "Laser-Induced Breakdown Spectroscopy," Anal. Chem. **85**, 640–669 (2013).

43. T. B. Lucatorto and T. J. McIlrath, "Efficient Laser Production of a Na+ Ground-State Plasma Column: Absorption Spectroscopy and Photoionization Measurement of Na+," Phys. Rev. Lett. **37**, 428–431 (1976).

44. C. G. Gill, T. M. Allen, J. E. Anderson, T. N. Taylor, P. B. Kelly, and N. S. Nogar, "Low-power resonant laser ablation of copper," Appl. Opt. **35**, 2069–2082 (1996).

45. J. K. Gibson, "Resonant Laser Ablation of Lanthanides: Eu and Lu Resonances in the 450−470 nm Region," Anal. Chem. **69**, 111–117 (1997).

46. C. J. McLean, J. H. Marsh, A. P. Land, A. Clark, R. Jennings, K. W. D. Ledingham, P. T. McCombes, A. Marshall, R. P. Singhal, and M. Towrie, "Resonant laser ablation (RLA)," Int. J. Mass Spectrom. Ion Process. **96**, R1–R7 (1990).

47. F. R. Verdun, G. Krier, and J. F. Muller, "Increased sensitivity in laser microprobe mass analysis by using resonant two-photon ionization processes," Anal. Chem. **59**, 1383–1387 (1987).

Journal of Analytical Atomic Spectrometry Accepted Manuscript

48. D. Cleveland, P. Stchur, X. Hou, K. X. Yang, J. Zhou, and R. G. Michel, "Resonant laser ablation of metals detected by atomic emission in a microwave plasma and by inductively coupled plasma mass spectrometry," Appl. Spectrosc. **59**, 1427–1444 (2005).

49. C. Vadla, V. Horvatic, D. Veza, and K. Niemax, "Resonantly laser induced plasmas in gases: The role of energy pooling and exothermic collisions in plasma breakdown and heating," Spectrochim. Acta Part B At. Spectrosc. **65**, 33–45 (2010).

50. G. C. Eiden, J. E. Anderson, and N. S. Nogar, "Resonant Laser Ablation: Semiquantitative Aspects and Threshold Effects," Microchem. J. **50**, 289–300 (1994).

51. K. Watanabe and T. Iguchi, "Modeling of vaporization processes of resonant laser ablation," Appl. Phys. A **69**, S845–S848 (1999).

52. C. G. Gill, A. W. Garrett, P. H. Hemberger, and N. S. Nogar, "Resonant laser ablation as a selective metal ion source for gas-phase ion molecule reactions," J. Am. Soc. Mass Spectrom. **7**, 664–667 (1996).

53. A. G. Shmakov, O. P. Korobeinichev, D. A. Knyazkov, A. A. Paletsky, R. A. Maksutov, I. E. Gerasimov, T. A. Bolshova, V. G. Kiselev, and N. P. Gritsan, "Combustion chemistry of Ti(OC3H7)4 in premixed flat burner-stabilized H2/O2/Ar flame at 1 atm," Proc. Combust. Inst. **34**, 1143–1149 (2013).

54. D. M. Schleich and B. Walter, "Formation of titania nanoparticles by vapor phase reactions of titanium tetraisopropoxide in oxygen/ozone containing atmospheres," Nanostructured Mater. **8**, 579–586 (1997).

55. S. Y. Kim, J. H. Yu, and J. S. Lee, "The characteristics of nanosized TiO_2 powders synthesized by chemical vapor condensation," Nanostructured Mater. **12**, 471–474 (1999).

56. H. Wu and L.-S. Wang, "Electronic structure of titanium oxide clusters: TiO_y (y= 1-3) and $(TiO_2)_n$ (n= 1-4)," J. Chem. Phys. **107**, 8221–8228 (1997).

Journal of Analytical Atomic Spectrometry Accepted Manuscript

57. N. Serpone, D. Lawless, and R. Khairutdinov, "Size Effects on the Photophysical Properties of Colloidal Anatase TiO2 Particles: Size Quantization versus Direct Transitions in This Indirect Semiconductor?," J. Phys. Chem. **99**, 16646–16654 (1995).

58. L. M. Cabalín and J. J. Laserna, "Experimental determination of laser induced breakdown thresholds of metals under nanosecond Q-switched laser operation," Spectrochim. Acta Part B At. Spectrosc. **53**, 723–730 (1998).

59. J. A. Stamper, K. Papadopoulos, R. N. Sudan, S. O. Dean, E. A. McLean, and J. M. Dawson, "Spontaneous magnetic fields in laser-produced plasmas," Phys. Rev. Lett. **26**, 1012–1015 (1971).

60. E. A. McLean, J. A. Stamper, C. K. Manka, H. R. Griem, D. W. Droemer, and B. H. Ripin, "Observation of magnetic fields in laser-produced plasma using the Zeeman effect," Phys. Fluids **27**, 1327–1335 (1984).

61. H. Lin, J. R. Kuhn, and R. Coulter, "Coronal Magnetic Field Measurements," Astrophys. J. **613**, L177–L180 (2004).

62. E. Stambulchik, K. Tsigutkin, and Y. Maron, "Spectroscopic Method for Measuring Plasma Magnetic Fields Having Arbitrary Distributions of Direction and Amplitude," Phys. Rev. Lett. **98**, 225001 (2007).

63. G. W. F. Drake, *Springer Handbook of Atomic, Molecular, and Optical Physics* (Springer, 2006).

64. R. B. Miles, W. R. Lempert, and J. NForkey, "Laser Rayleigh scattering," Meas. Sci. Technol. **12**, R33 (2001).

65. J. A. Stamper, "Review on spontaneous magnetic fields in laser-produced plasmas: Phenomena and measurements," Laser Part. Beams **9**, 841–862 (1991).

66. R. Serov and M. C. Richardson, "Measurement of intense magnetic fields associated with laser−produced plasmas," Appl. Phys. Lett. **28**, 115–118 (1976).

67. M. Corsi, G. Cristoforetti, M. Giuffrida, M. Hidalgo, S. Legnaioli, L. Masotti, V. Palleschi, A. Salvetti, E. Tognoni, C. Vallebona, and A. Zanini, "Archaeometric Analysis of Ancient Copper

Journal of Analytical Atomic Spectrometry Accepted Manuscript

Artefacts by Laser-Induced Breakdown Spectroscopy Technique," Microchim. Acta **152**, 105–111 (2005).

68. A. Giakoumaki, K. Melessanaki, and D. Anglos, "Laser-induced breakdown spectroscopy (LIBS) in archaeological science—applications and prospects," Anal. Bioanal. Chem. **387**, 749–760 (2007).

69. D. Menut, P. Fichet, J.-L. Lacour, A. Rivoallan, and P. Mauchien, "Micro-laser-induced breakdown spectroscopy technique: a powerful method for performing quantitative surface mapping on conductive and nonconductive samples," Appl. Opt. **42**, 6063–6071 (2003).

70. A. Dogariu, J. B. Michael, M. O. Scully, and R. B. Miles, "High-Gain Backward Lasing in Air," Science **331**, 442–445 (2011).

71. A. Sharma, N. D. Bhaskar, Y. Q. Lu, and W. Happer, "Continuous-wave mirrorless lasing in optically pumped atomic Cs and Rb vapors," Appl. Phys. Lett. **39**, 209–211 (1981).

72. H. Ninomiya and K. Hirata, "Laser action of optically pumped atomic titanium vapor," J. Appl. Phys. **66**, 2219–2220 (1989).

73. H. Ninomiya and K. Hirata, "Visible laser action in N2-laser-pumped Ti vapor," J. Appl. Phys. **68**, 5378–5380 (1990).

74. K. Hirata, S. Yoshino, and H. Ninomiya, "Optically pumped titanium vapor laser at 551.4 nm," J. Appl. Phys. **67**, 45–48 (1990).

75. H. Ninomiya, K. Hirata, and S. Yoshino, "Optically pumped titanium vapor laser at 625.8 nm," J. Appl. Phys. **66**, 3961–3962 (1989).

Journal of Analytical Atomic Spectrometry Accepted Manuscript

Figures:

Figure Captions list:

Fig. 1. Schematic of stagnation swirl flame synthesis setup. TEM of nanoparticles collected on substrate from the setup shows ~10nm particle size, where the scale bar is 20 nm.

Fig. 2. Schematic of the PS-LIBS setup.

Fig. 3. Spectra of emissions (around 500 nm) from PS-LIBS of titania nanoparticles at 14mm distance from the burner from (a) 532 nm and (b) 355 nm laser excitations, with the same excitation laser irradiance (2.4 GW/cm^2). The lines correspond to the NIST data for Ti.

Fig. 4. Partial Grotrian diagram of the energy levels of titanium atoms involved in '355' nm resonant excitation and corresponding emissions at 497.534nm and 480.541nm.

Fig. 5. Integrated emission intensity along centerline axis of synthesis flow for 532 nm and 355 nm laser excitations. The computed diameter is also displayed to indicate the expected phase-change or particle growth along the axis.

Fig. 6. Emission intensity change for 497.534 nm and other emissions with laser irradiance at 355nm excitation. Inset shows the intensity change with laser irradiance at 532nm excitation.

Fig. 7. Temporal evolution of the emission spectrum from 2.5 to 32.5 ns relative delay time for 355nm laser irradiance of 2.4 GW/cm^2.

Journal of Analytical Atomic Spectrometry Accepted Manuscript

Fig. 8. Temporal evolution of the emission spectrum from -7.5 to 2.5 ns relative delay time, showing the peak split and convergence centered at 497.534nm. Note: 0ns relative delay time corresponds to the peak of the excitation laser pulse. The inset plots the center wavelength of emission peaks converging to 497.543nm from -7.5 to 7.5 ns relative delay time.

Fig 9. Temporal evolution of the emissions around 497.534 for different wavelengths using PMT, for 355nm laser excitation.

Fig. 10. Relative time (with respect to the laser pulse peak) for emissions near 497.534 to reach peak value.

Fig. 11. Temporal evolution of peak width (FWHM) of 497.534 nm emission for excitation with unseeded laser. The inset shows the cumulative spectrum collected from -10ns to -5 ns relative delay time.

Fig. 12. Emissions at different excitation laser wavelengths, with resonance at 282.347nm.

Journal of Analytical Atomic Spectrometry Accepted Manuscript

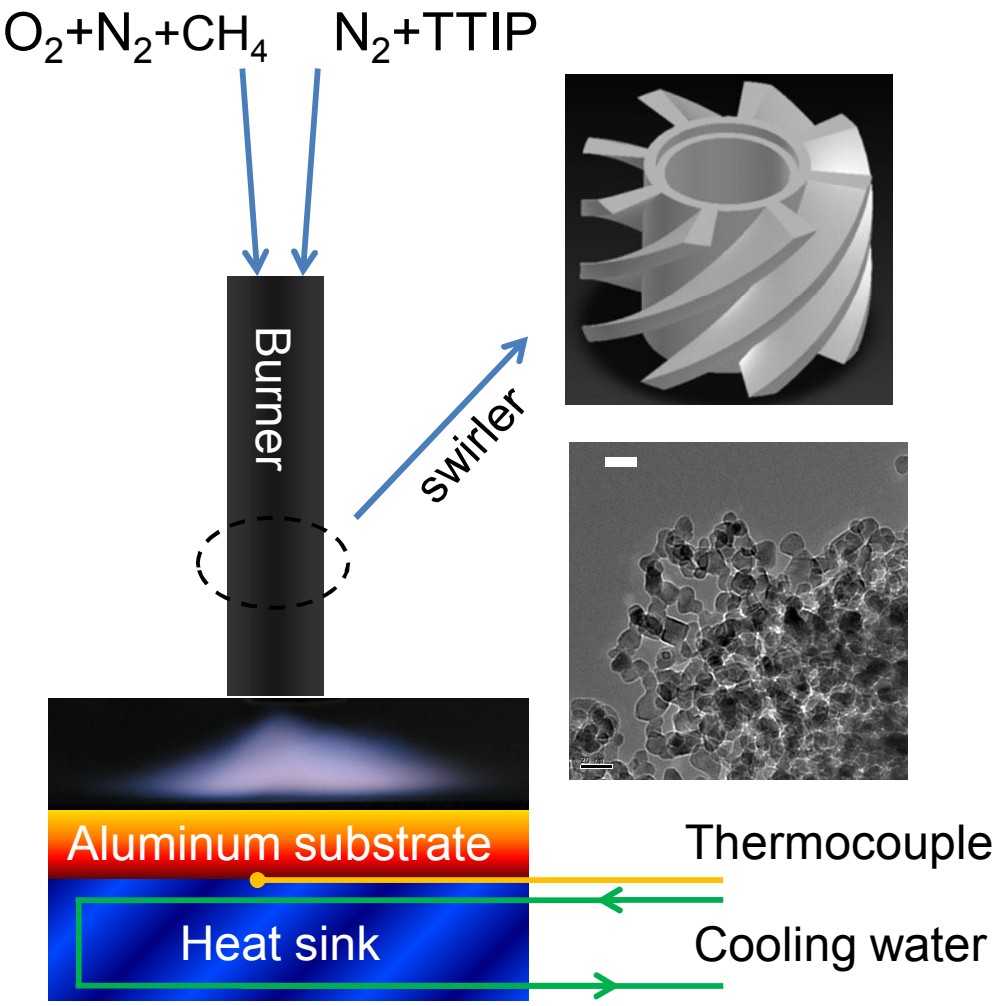

Fig. 1. Schematic of stagnation swirl flame synthesis setup. TEM of nanoparticles collected on substrate from the setup shows ~10nm particle size, where the scale bar is 20 nm.

Journal of Analytical Atomic Spectrometry Accepted Manuscript

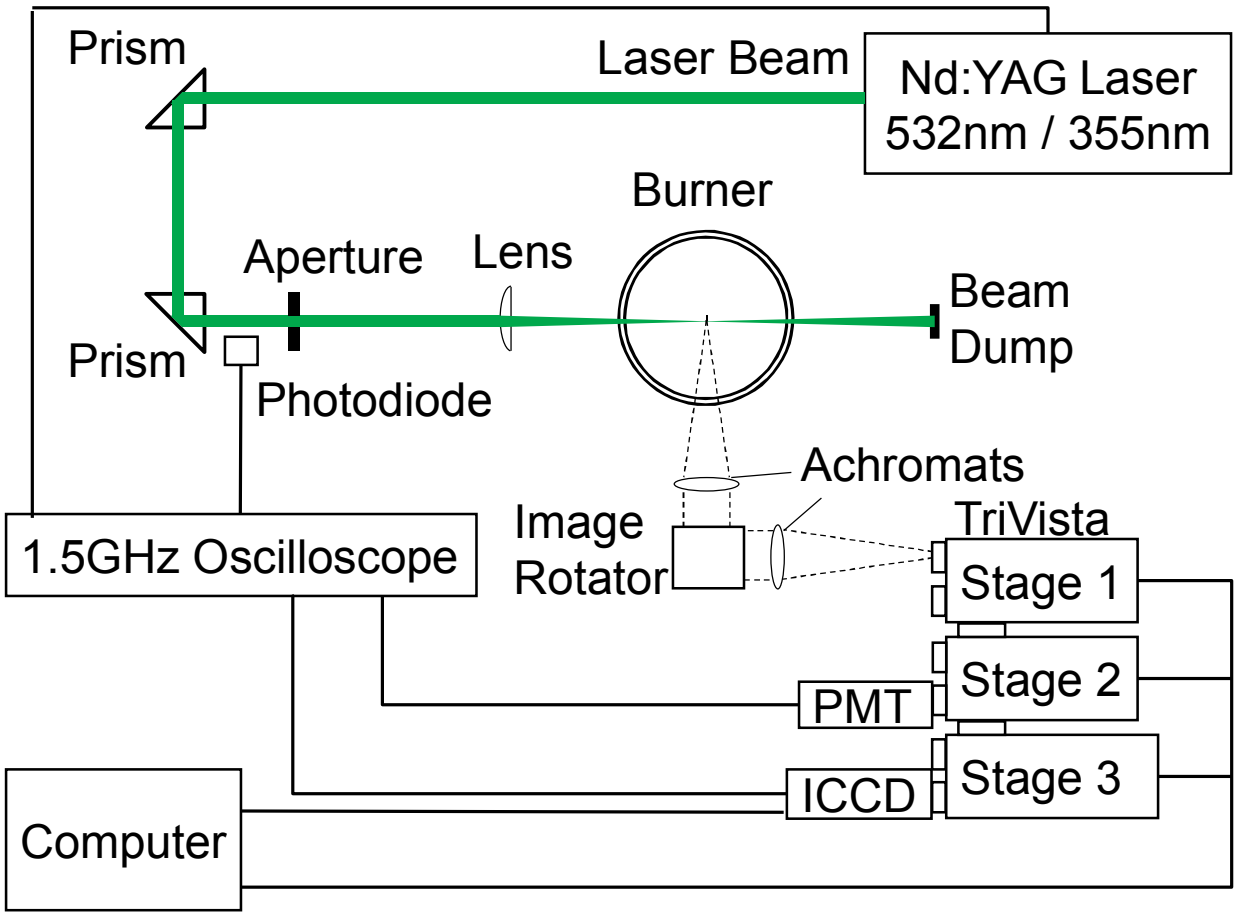

Fig. 2. Schematic of the PS-LIBS setup.

Journal of Analytical Atomic Spectrometry Accepted Manuscript

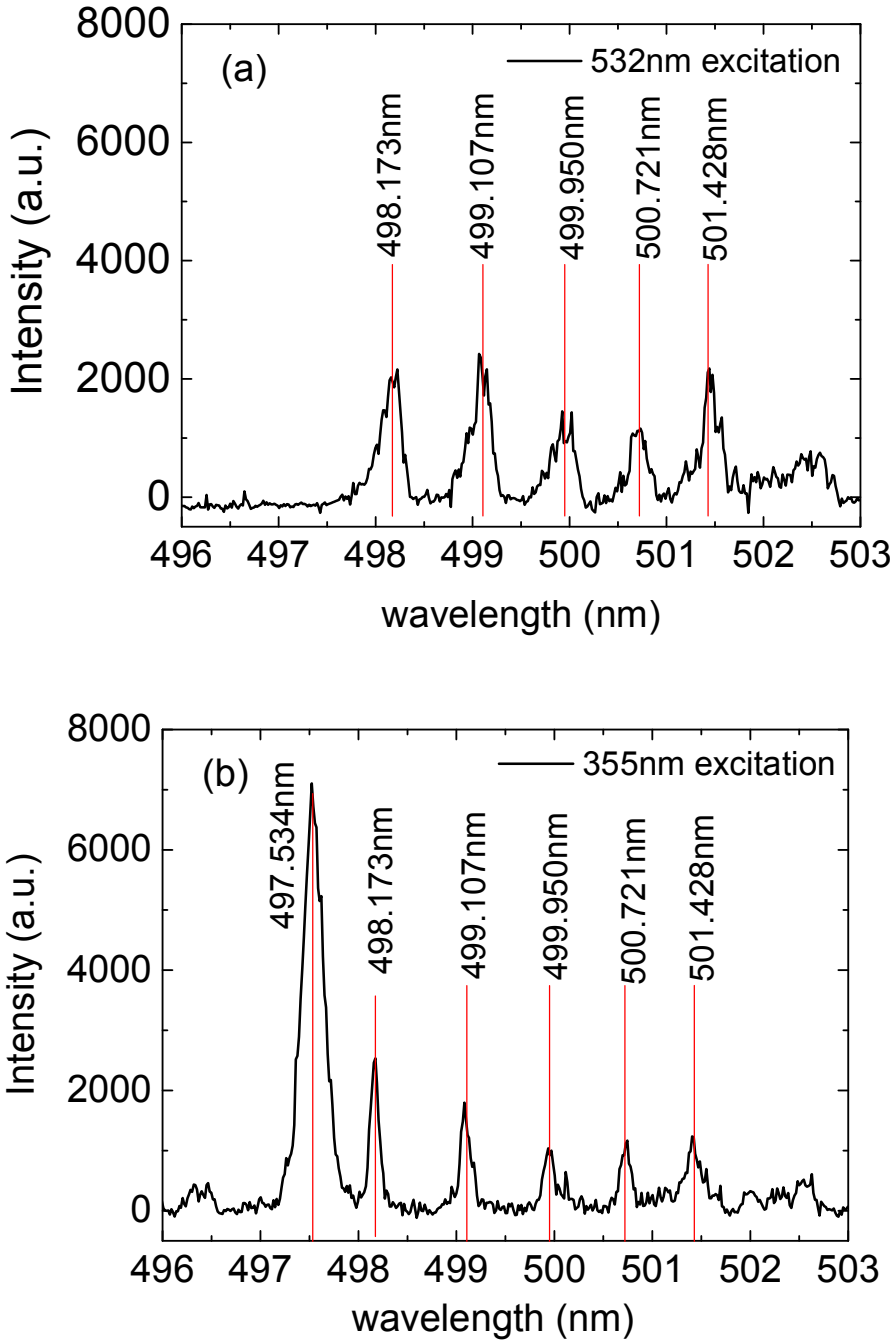

Fig. 3. Spectra of emissions (around 500nm) from PS-LIBS of titania nanoparticles at 14mm distance from the burner from (a) 532 nm and (b) 355 nm laser excitations, with the same excitation laser irradiance (2.4 GW/cm^2). The lines correspond to the NIST data for Ti.

Journal of Analytical Atomic Spectrometry Accepted Manuscript

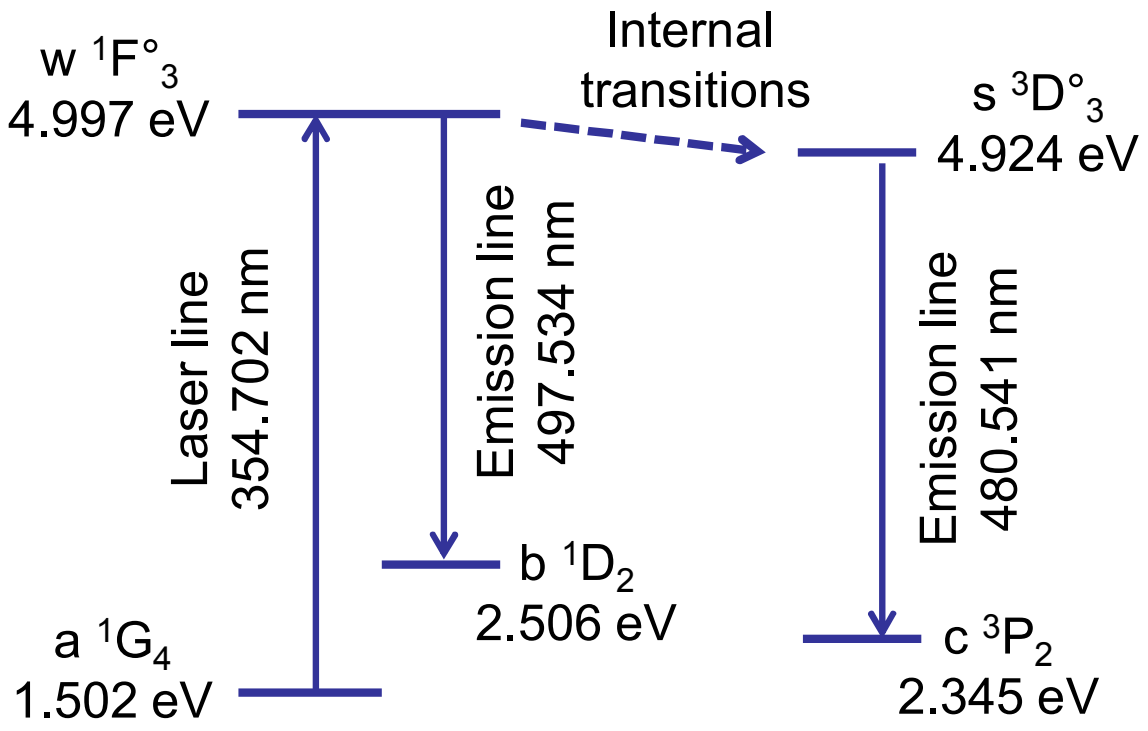

Fig. 4. Partial Grotrian diagram of the energy levels of titanium atoms involved in '355' nm resonant excitation and corresponding emissions at 497.534nm and 480.541nm.

Journal of Analytical Atomic Spectrometry Accepted Manuscript

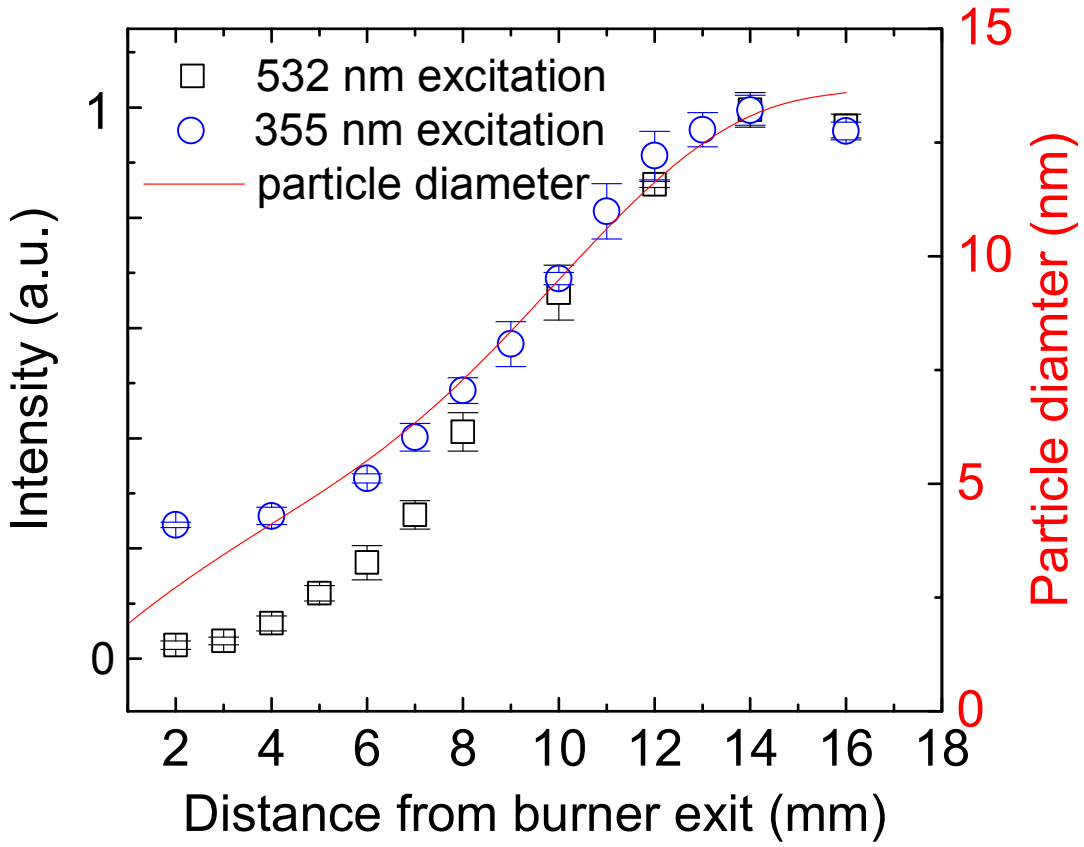

Fig. 5. Integrated emission intensity along centerline axis of synthesis flow for 532 nm and 355 nm laser excitations. The computed diameter is also displayed to indicate the expected phase-change or particle growth along the axis.

Journal of Analytical Atomic Spectrometry Accepted Manuscript

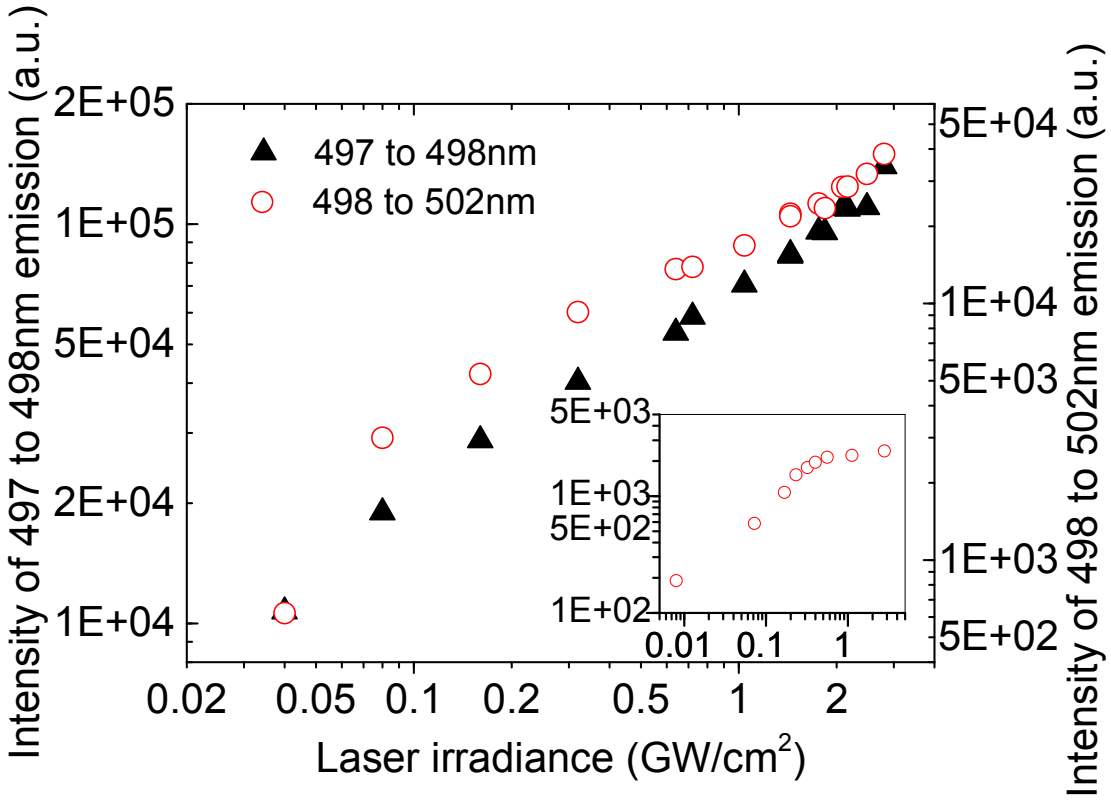

Fig. 6. Emission intensity change for 497.534 nm and other emissions with laser irradiance at 355nm excitation. Inset shows the intensity change with laser irradiance at 532nm excitation.

Journal of Analytical Atomic Spectrometry Accepted Manuscript

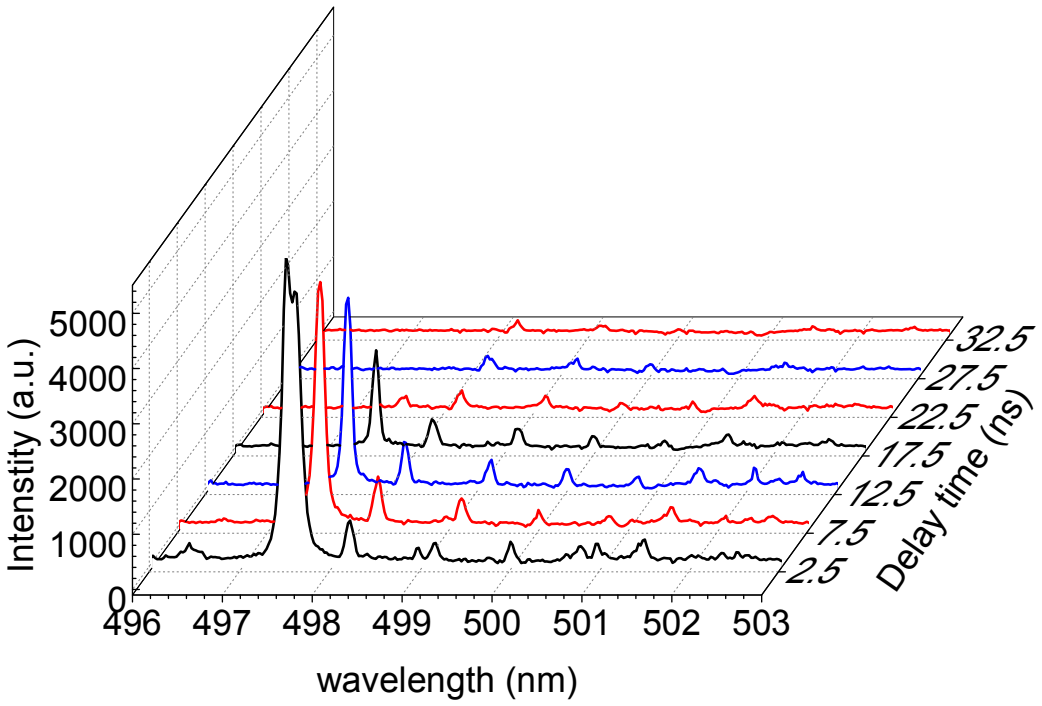

Fig. 7. Temporal evolution of the emission spectrum from 2.5 to 32.5 ns relative delay time for 355nm laser irradiance of 2.4 GW/cm^2.

Journal of Analytical Atomic Spectrometry Accepted Manuscript

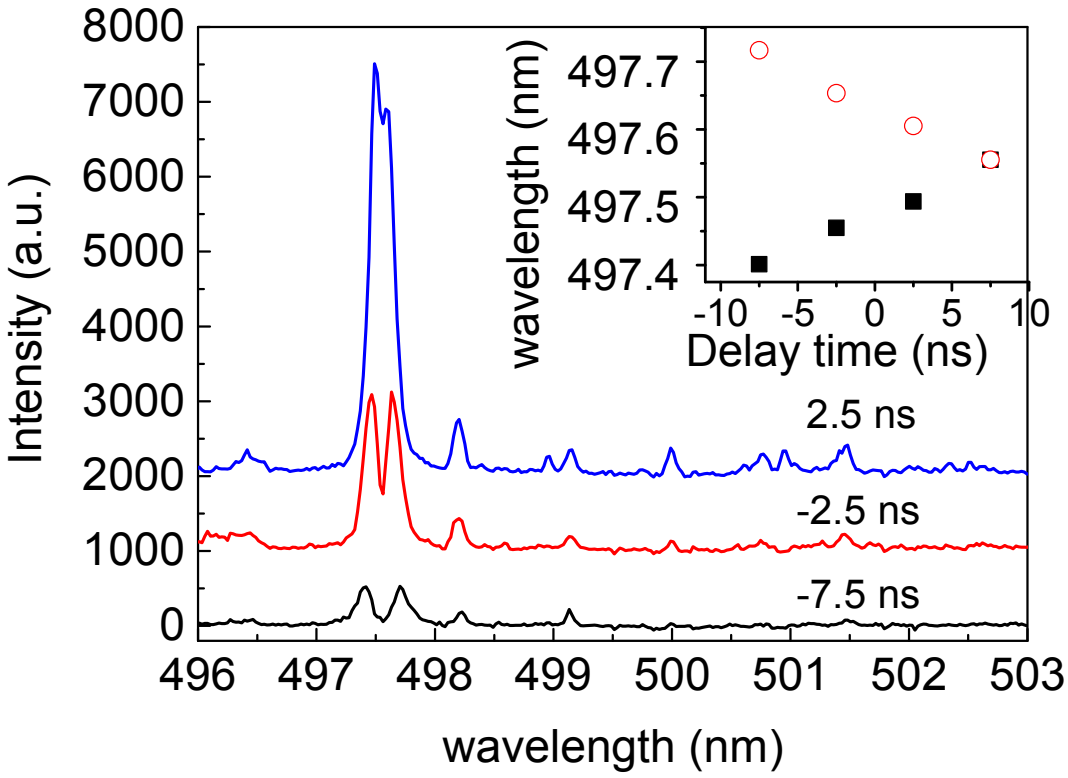

Fig. 8. Temporal evolution of the emission spectrum from -7.5 to 2.5 ns relative delay time, showing the peak split and convergence centered at 497.534nm. Note: 0ns relative delay time corresponds to the peak of the excitation laser pulse. The inset plots the center wavelength of emission peaks converging to 497.543nm from -7.5 to 7.5 ns relative delay time.

Journal of Analytical Atomic Spectrometry Accepted Manuscript

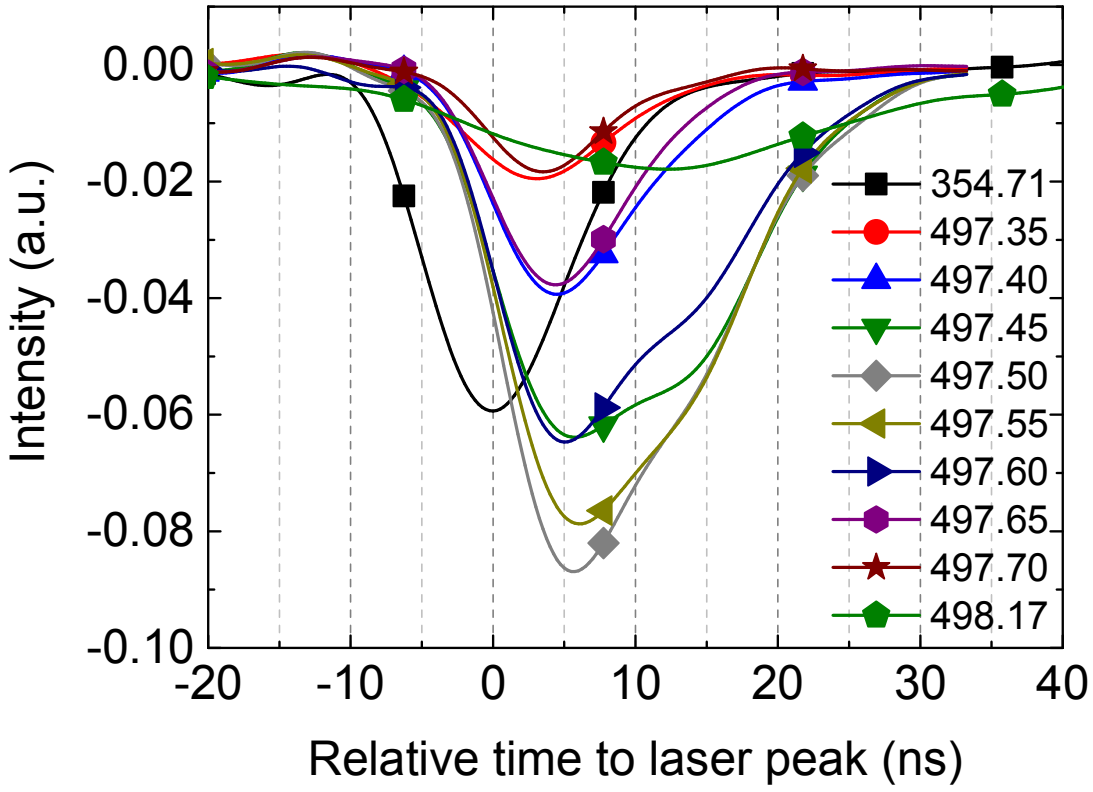

Fig. 9. Temporal evolution of the emissions around 497.534 for different wavelengths using PMT, for 355nm laser excitation.

Journal of Analytical Atomic Spectrometry Accepted Manuscript

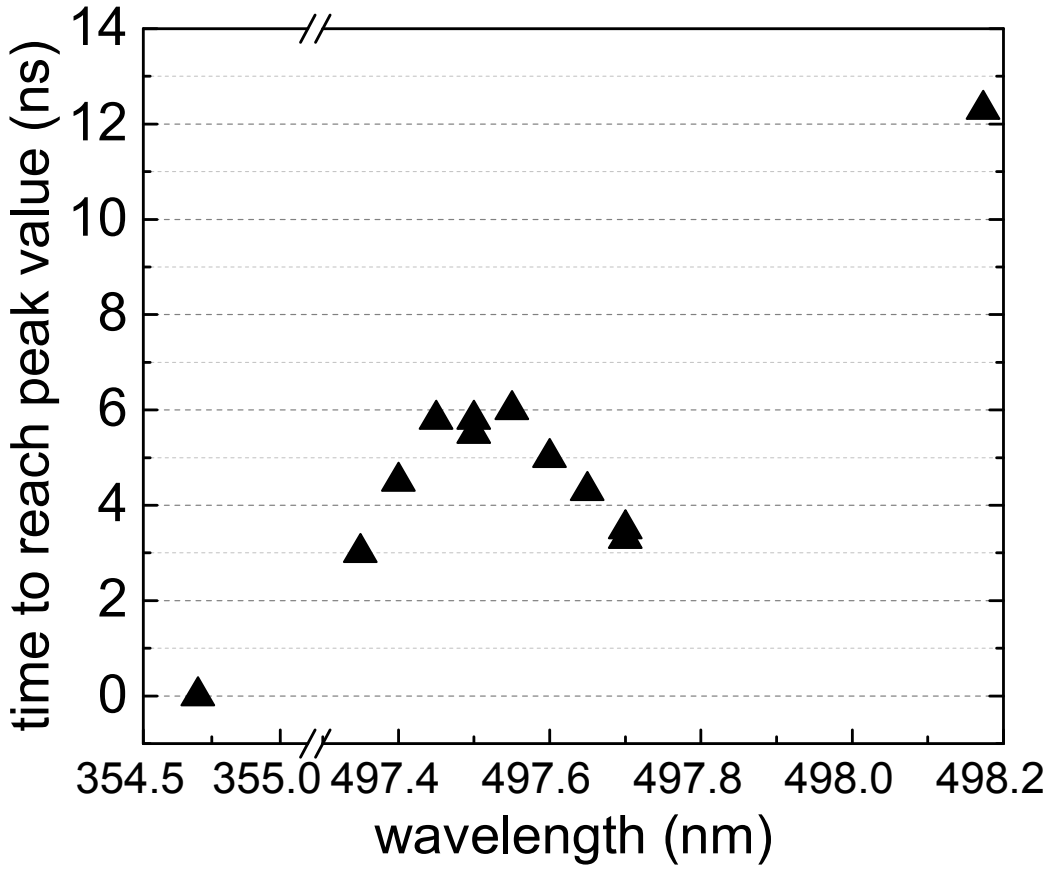

Fig. 10. Relative time (with respect to the laser pulse peak) for emissions near 497.534 to reach peak value.

Journal of Analytical Atomic Spectrometry Accepted Manuscript

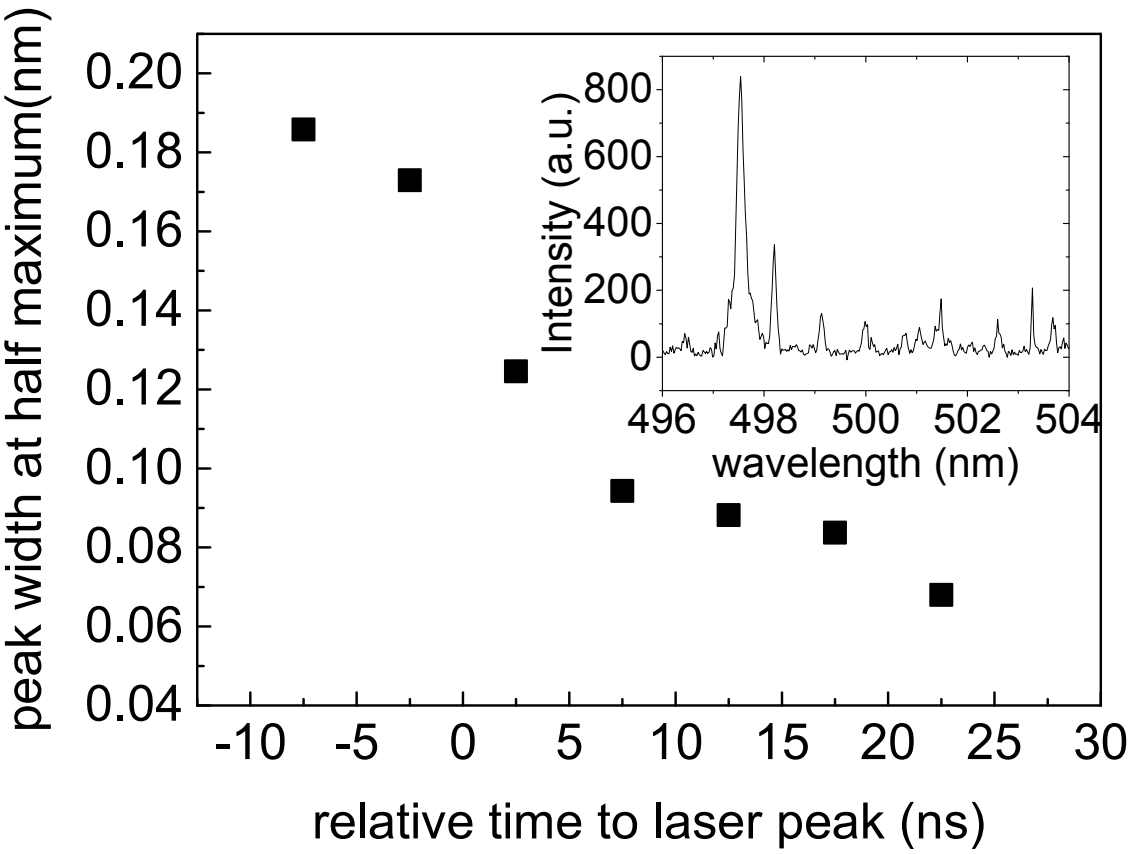

Fig. 11. Temporal evolution of peak width (FWHM) of 497.534 nm emission for excitation with unseeded laser. The inset shows the cumulative spectrum collected from -10ns to -5 ns relative delay time.

Journal of Analytical Atomic Spectrometry Accepted Manuscript

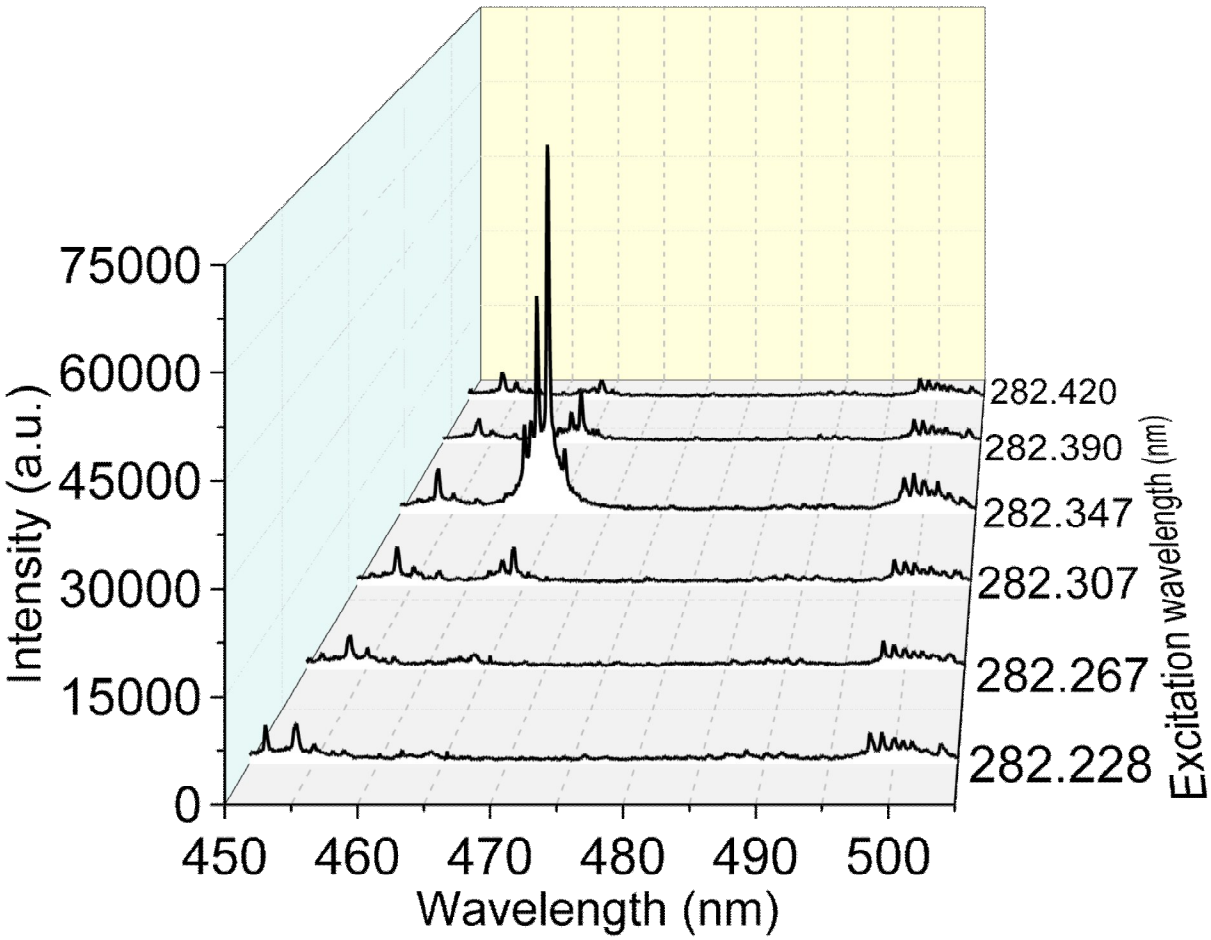

Fig. 12. Emissions at different excitation laser wavelengths, with resonance at 282.347nm.

Journal of Analytical Atomic Spectrometry Accepted Manuscript